Check for updates

Angewandte Chemie International Edition

Angewandte International Edition Chemie

How to cite: *Angew. Chem. Int. Ed.* **2026**, e7709103
doi.org/10.1002/anie.7709103

RESEARCH ARTICLE

Record-High Toroidal Blocking in a $\{Cu_6Dy_3\}$ Single Molecular Toroid

Deepanshu Chauhan[1] | Jan Arneth[2] | Sagar Paul[3] | Bapan Jana[1] | Wolfgang Wernsdorfer[3] | Rüdiger Klingeler[2] | Maheswaran Shanmugam[1] | Gopalan Rajaraman[1]

[1]Department of Chemistry, Indian Institute of Technology Bombay, Mumbai, India | [2]Kirchhoff Institute for Physics, Heidelberg University, Heidelberg, Germany | [3]Institute for Quantum Materials and Technology, Karlsruhe Institute of Technology (KIT), Karlsruhe, Germany

Correspondence: Jan Arneth (jan.arneth@kip.uni-heidelberg.de) | Sagar Paul (sagar.paul@kit.edu) | Wolfgang Wernsdorfer (wolfgang.wernsdorfer@kit.edu) | Rüdiger Klingeler (klingeler@kip.uni-heidelberg.de) | Maheswaran Shanmugam (eswar@chem.iitb.ac.in) | Gopalan Rajaraman (rajaraman@chem.iitb.ac.in)

Received: 4 June 2026 | **Revised:** 21 October 2026 | **Accepted:** 26 October 2026

Keywords: condensed matter physics | electron paramagnetic resonance | exchange interaction | ferromagnetism | nanomagnet | quantum | quantum decoherence | toroid | Single molecule toroid | toroidal moment

ABSTRACT

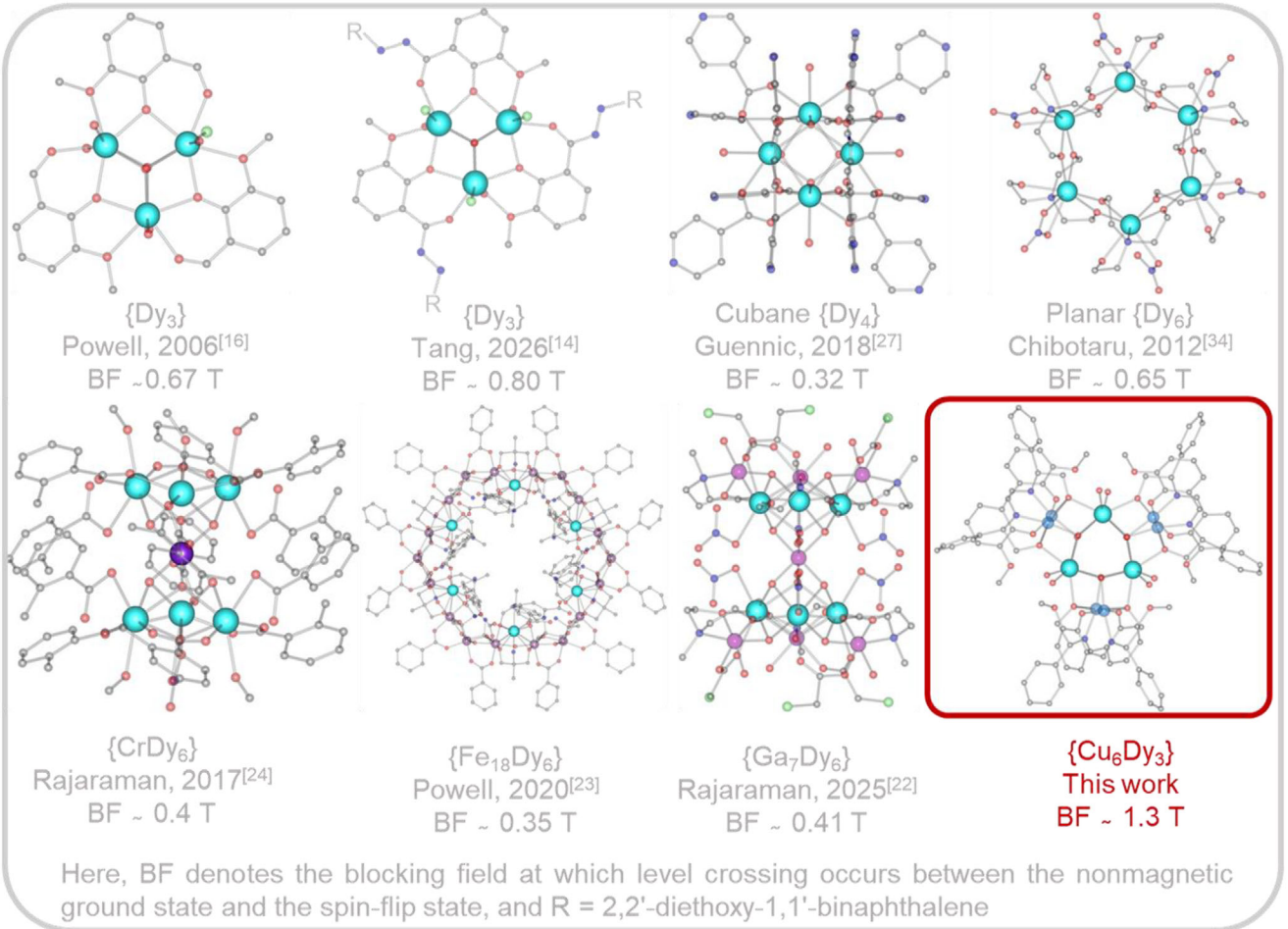
Single-molecule toroids (SMTs) are promising for quantum technologies because their vortex-like spin arrangement generates magnetically silent ground states with minimal stray fields and enhanced protection against decoherence. However, their technological potential requires toroidal states that remain stable under strong external magnetic fields, since weak intramolecular interactions can induce spin flips and destroy toroidal order. In this study, we report heterometallic {3d–4f} complexes, $[Ln_3Cu_6L_6(\mu_3\text{-}OH)_6(\mu_1\text{-}H_2O)_6]^{3+}$ (Ln = Dy (**1**), Y (**2**); L^{2-} = (S,E)-*N*-(2-(λ^1-oxidaneyl)-1-phenylethyl)-1-(3-methoxy-2-(λ^1-oxidaneyl)phenyl)ethan-1-imine)). Remarkably, the Dy(III) analogue retains its magnetically silent toroidal ground state up to 1.3 T, establishing an unprecedented benchmark for toroidal magnetization blocking and extending the field stability of molecular toroidal states beyond previous limits. Sub-kelvin μ-SQUID measurements, high-frequency EPR spectroscopy, and theoretical modelling show that this high blocking field originates from an unexpectedly strong Dy–Dy exchange interaction, suggested to arise from neighboring Cu(II) ions, whereas direct ferromagnetic Cu–Dy exchange weakly destabilizes the toroidal state. These results reveal a new strategy for stabilizing toroidal states at high fields through targeted control of intramolecular exchange interactions, opening opportunities for electrically addressable molecular nanomagnets and quantum technologies.

1 | Introduction

The realization of magnetic states that combine stability, controllability, and minimal magnetic noise is a central challenge in molecular magnetism [1–3]. Conventional single-molecule magnets (SMMs) [4–6], based on bistable magnetic ground states, have advanced the understanding of molecular spin dynamics; however, their intrinsic net magnetic moment generates stray fields and dipolar interactions, leading to decoherence and limiting their scalability in high-density and quantum-device architectures [7–11].

Magnetically silent ground states, in which internal spin order exists without a net magnetic dipole moment, offer an attractive alternative [12–14]. By suppressing dipolar interactions, such states minimize magnetic cross-talk and provide enhanced robustness against environmental perturbations [15]. Among these, single-molecule toroids (SMTs) represent a unique class,

All rights reserved, including rights for text and data mining and training of artificial intelligence technologies or similar technologies.
© 2026 Wiley-VCH GmbH



SCHEME 1 | A schematic comparison of the blocking field (BF) reported for related complexes in the literature, together with the present work.

where local magnetic moments form a closed loop, giving rise to a toroidal moment while maintaining zero net magnetization [16–18]. This "hidden" magnetic order couples to electric fields, enabling magnetoelectric responses and offering potential for electrically addressable spin states [19].

Over the past two decades, significant progress has been made in the design of lanthanide-based SMTs, particularly in triangular $\{Dy_3\}$ motifs where strong single-ion anisotropy and tangential orientation of local easy axes naturally generate toroidal ground states [18, 20, 21]. A variety of structural strategies, including ligand-field engineering, symmetry control, and modulation of intramolecular interactions, have been employed to stabilize such states and suppress quantum tunneling of magnetization [22–24]. These efforts have led to increasingly well-defined toroidal systems, along with experimental signatures such as slow magnetic relaxation, characteristic hysteresis features, and distinct spectroscopic fingerprints [25, 26]. Despite these advances, the stability of toroidal states under external magnetic fields remains fundamentally limited, with blocking fields typically not exceeding ~0.8 T (Scheme 1) [14, 16, 22, 23, 27–34]. This limitation reflects the absence of mechanisms analogous to exchange-enhanced blocking in conventional SMMs, where strong intramolecular coupling plays a decisive role in suppressing quantum tunneling [35–37]. While exchange bias has been successfully exploited in magnetically active systems such as metallocenes [4], dimers [38, 39], and metal–radical complexes [40], its application to magnetically silent toroidal systems remains largely unexplored.

In this study, we investigate the influence of exchange bias on a toroidal moment in the heterometallic {3d–4f} complexes, $[Ln_3Cu_6L_6(\mu_3\text{-}OH)_6(\mu_1\text{-}H_2O)_6]\cdot Cl_3\cdot 2H_2O\cdot 2MeOH\cdot 2MeCN$ (where, Ln = Dy (**1**), Y (**2**), and L^{2-} = (S,E)-*N*-(2-(λ^1-oxidaneyl)-1-phenylethyl)-1-(3-methoxy-2-(λ 1-oxidaneyl)phenyl)ethan-1-imine)), featuring an exchange-coupled $\{Cu_3–Ln_3–Cu_3\}$ architecture. The $\{Dy_3\}$ analogue is shown to exhibit both single-molecule magnet and toroidal behavior. The exchange-active $\{Cu_3\}$ units are found to generate an internal bias field that suppresses quantum tunneling, but destabilizes the toroidal ground state. Nonetheless, an enhanced magnetic Dy(III)–Dy(III) exchange results in toroidal blocking persisting to unprecedentedly high magnetic fields of 1.3T.

2 | Result and Discussion

2.1 | Synthesis and Structure Descriptions

The ligand LH_2 was reacted with $LnCl_3\cdot 6H_2O$ (Ln = Dy (**1**), Y (**2**)) in methanol in the presence of Et_3N, followed by the addition of $Cu(ClO_4)_2\cdot 6H_2O$, yielding green crystals suitable for x-ray diffraction via slow evaporation (MeOH/MeCN). Both complexes

15213773, 0, Downloaded from https://onlinelibrary.wiley.com/doi/10.1002/anie.7709103 by Rüdiger Klingeler - Universitatsbibliothek Heidelberg , Wiley Online Library on [06/11/2026]. See the Terms and Conditions (https://onlinelibrary.wiley.com/terms-and-conditions) on Wiley Online Library for rules of use; OA articles are governed by the applicable Creative Commons License

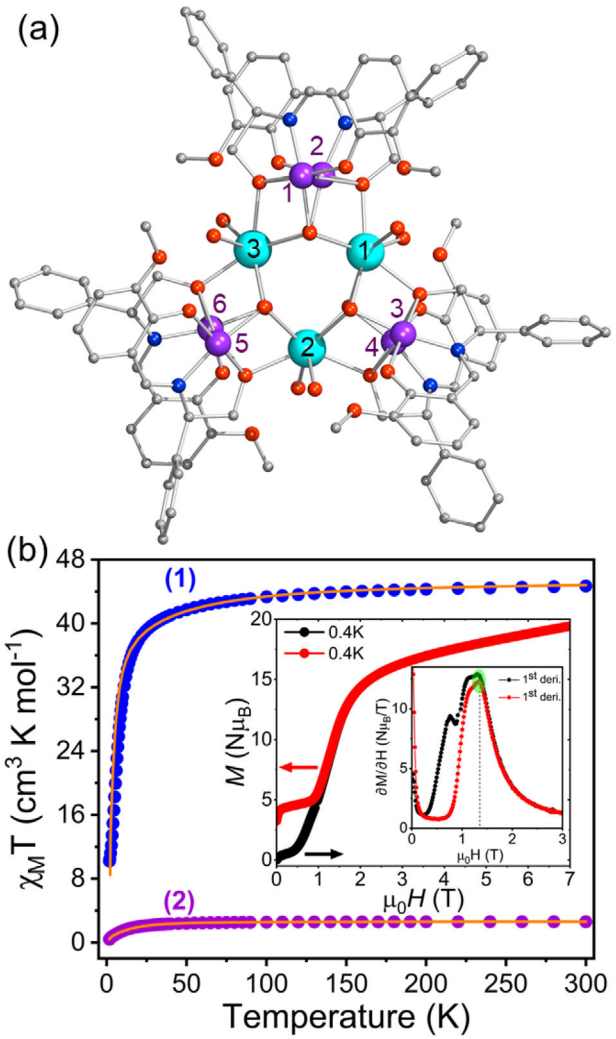


FIGURE 1 | (a) Molecular structure of the complex **1** showing the metal core and coordination environment; Hydrogen atoms are omitted for clarity. Color code: Dy, cyan; Cu, purple; O, red; N, blue; C, grey. (b) Temperature dependence of the magnetic susceptibility (χ_MT) for both the complexes at 0.1T; experimental data (dots) and fitted curves (solid lines, obtained from Poly_Aniso). The inset presents the field-dependent magnetization at 0.4 K and its first derivative, revealing a field-induced magnetic transition.

crystallize in the orthorhombic space group $P2_12_12_1$ and are isostructural (synthesis procedure in Supporting Information and Table S1 for crystallographic parameters). Complex **1** consists of a cationic $\{Dy_3Cu_6\}^{3+}$ cluster, charge-balanced by three chloride anions, along with solvent molecules. The structure features a triangular $\{Dy_3\}$ core, with each Dy–Dy edge bridged by a $\{Cu_2L_2\}$ unit, forming a $\{Cu_3–Dy_3–Cu_3\}$ architecture (Figure 1a), in which three Cu(II) ions are located above and three below the $\{Dy_3\}$ plane, each set of three forming a $\{Cu_3\}$ triangle. The framework is supported by μ_3-OH and alkoxo bridges, generating distorted cubane-like $\{Dy_2Cu_2O_4\}$ subunits fused via shared Dy(III) vertices. Each Dy(III) ion adopts an eight-coordinate, approximately square-antiprismatic geometry, while the Cu(II) centers exhibit distorted square-pyramidal coordination environments (Table S2). The Dy···Dy and Dy···Cu separations are ~3.8 Å and ~3.3–3.8 Å, respectively, supporting efficient magnetic communication within the cluster. Further crystallographic details, including bond lengths, angles, and coordination metrics, are provided in Tables S3 and S4. Phase purity of the bulk sample was confirmed by powder x-ray diffraction (PXRD), which shows good agreement between the experimental pattern and that simulated from the single-crystal structure (Figure S1).

2.2 | Basic Magnetic Characterization

Direct current (DC) magnetic susceptibility measurements for complexes **1**–**2** were performed in the temperature range 1.8–300 K under an applied field of 0.1 T (Figure 1b). At 300 K, the χ_mT values of 44.69 cm^3 K mol^{-1} (**1**) and 2.60 cm^3 K mol^{-1} (**2**) agree well with the expected values for six Cu(II) ions with g = 2.15 and three Dy(III) or diamagnetic Y(III) ions, respectively. For complex **1**, χ_mT remains nearly constant down to ~100 K. Below this temperature, a gradual decrease, followed by a sharp drop below ~20 K, is observed, which likely arises from the depopulation of the Dy(III) m_J sublevels [41]. The overall behavior is consistent with strong magnetic anisotropy and weak intramolecular exchange. Qualitatively, complex **2** exhibits a similar χ_mT-profile as **1** (Figure S2 for an enlarged view). However, due to the absence of multiplet splitting in the Cu(II) ions, the gradual decrease already at intermediate temperatures indicates the presence of sizable antiferromagnetic coupling within the Cu(II) framework. Consequently, such interactions are also present in **1** but masked by the magnetic contribution of the Dy(III) ions.

Field-dependent magnetization (M vs. H) measurements (1.8–8 K, up to 7 T) show that complex **1** exhibits a weak but rapid increase in magnetization at low magnetic fields, followed by a clear convex-upward (S-shaped) behavior (Figure S3). At 1.3 T, a point of inflection signals the stabilization of a new magnetic ground state. The low-temperature (1.8 K) magnetization reaches 20.3 $N\mu_B$, that is, no full saturation, at 7 T, consistent with strong axial magnetic anisotropy. The observed level crossing becomes even better visible when further lowering the temperature to 0.4 K (inset of Figure 1b). At such low temperatures, complex **1** shows a distinct S-shaped magnetization curve with a suppressed low-field response, indicative of a magnetically silent (toroidal) ground state [16, 18]. The sharp increase of the magnetization at μ_0H_C = 1.3 T is consistent with a field-induced transition from a toroidal state to a magnetic spin-flip state. Below μ_0H_C, the magnetization loop exhibits pronounced hysteresis. As for complex **2**, $M(H, T = 0.4\ K)$ also displays a clear S-shape, signaling a level crossing from a magnetically almost silent to a $S = 1$ ($M \approx 2\ N\mu_B$) ground state at 2.4 T (Figure S2). Up to 7 T, the magnetization does not fully saturate but reaches 2.07 $N\mu_B$. Overall, the magnetic behavior is in line with considerable antiferromagnetic coupling, as discussed earlier.

2.3 | Detection of Toroidal States via μSQUID Measurements

To further elucidate the ground states of complexes **1** and **2**, sub-Kelvin magnetization measurements were performed on oriented single crystals (~50 μm) using μSQUID magnetometry. As already evident from the bulk SQUID data at 0.4 K, complex **1** exhibits clear open magnetic hysteresis loops when the field is applied

15213773, 0, Downloaded from https://onlinelibrary.wiley.com/doi/10.1002/anie.7709103 by Rüdiger Klingeler - Universitatsbibliothek Heidelberg , Wiley Online Library on [06/11/2026]. See the Terms and Conditions (https://onlinelibrary.wiley.com/terms-and-conditions) on Wiley Online Library for rules of use; OA articles are governed by the applicable Creative Commons License

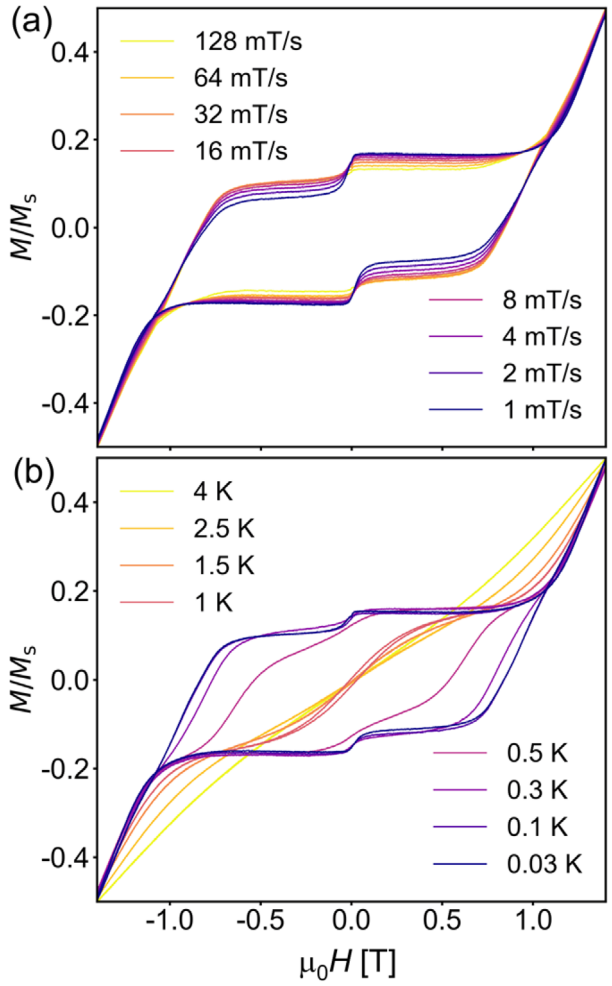


FIGURE 2 | Scaled *M(H)* curves for a single crystal of **1** with field along its easy axis, obtained by μSQUIDs at 30 mK temperature with varying sweep rates (a), and at a fixed sweep rate of 16 mT/s with varying temperatures (b).

along an easy axis within the measurement plane (Figures 2 and S4), thereby revealing the intrinsic single-molecule magnetic behavior. At 30 mK, the sweep-rate-dependent *M(H)* curves (Figure 2a) display a characteristic constricted hysteresis in the low-field region, indicative of a non-collinear toroidal ground state in which the net magnetic moment is largely compensated by the vortex-like arrangement of the Dy(III) anisotropy axes. A sharp step-like transition appears at $\mu_0 H_C = 1.3$ T, corresponding to the field-induced conversion from the toroidal to a field-polarized spin-flip state. The hysteresis broadens progressively with increasing sweep rate, reflecting slow magnetization dynamics governed by phonon-assisted quantum tunneling of the magnetization (QTM) even at millikelvin temperatures.

Temperature-dependent measurements collected at a fixed sweep rate of 16 mT/s (Figure 2b) further demonstrate that magnetic hysteresis remains nearly unchanged below 0.5 K, consistent with relaxation dominated by QTM. Above this temperature, the coercive field and loop area gradually decrease due to thermally activated relaxation processes, and the hysteresis disappears above ~1.5 K. Notably, the magnetization does not fully saturate within the accessible field range (±1.4 T), in agreement with the strong magnetic anisotropy of Dy(III) and the persistence of toroidal correlations. Importantly, the critical blocking field ($\mu_0 H_C = 1.3$ T) is significantly larger than those reported for most Dy(III)-based single-molecule toroics, including the archetypal {Dy_3} triangle (Figure S5).

In contrast, the μSQUID measurements for complex **2** (Figure S6) show magnetic behavior indicative of an $S = 0$ ground state, without any evidence of toroidal magnetic ordering. This is consistent with dominant intratriangular antiferromagnetic exchange interactions between the Cu(II) ions, as supported by bulk magnetic measurements and ab initio calculations.

2.4 | Slow Relaxation Dynamics of the Toroidal State

Complementing the AC susceptibility measurements on powder samples at higher temperatures, magnetization relaxation measurements at sub-Kelvin temperatures were also obtained using μSQUID magnetometry on an oriented single crystal. Following a sweep from maximum field to zero field, DC magnetization decay curves were recorded at various bath temperatures (Figure 3a). Individual relaxation times were extracted by scaling these temperature-dependent curves to a master curve (Figure 3b) after normalizing time to a dimensionless t/τ axis. At such low temperatures, the presence of multiple competing parallel and serial relaxation pathways can lead to deviations from conventional stretched exponential behavior [22, 42]. Consequently, scaling to a master curve (Figure 3b) provides a more general framework to extract temperature-dependent mean relaxation times. The resulting relaxation times (τ), combined with those from AC susceptibility data (Figure 3c), are plotted as a function of $1/T$ in Figure 3d. To minimize fitting parameters, the high-temperature region (AC data) was first fitted using a linear relation, $ln(\tau) = ln\tau_0 + U_{eff}/k_B T$, yielding $U_{eff}/k_B = 35$ (2) K and $\tau_0 = 10^{-9.8(3)}$. Fixing these values, a generalized fit incorporating Orbach, Raman, and QTM processes [39], $ln(\tau) = -ln[\tau_0^{-1} exp(-U_{eff}/k_B T) + CT^n + 1/\tau_Q]$, gave a Raman exponent $n \approx 8.8$ (9) and a QTM relaxation time $\tau_Q = 1.66\ (69) \times 10^4$ s. Notably, τ_Q lies within the upper range of values reported for {Dy_3}-based systems, suggesting that strongly quenched three-body tunnelling between clockwise and anticlockwise {Dy_3} toroidal states at zero field may be further suppressed, for which the Dy-Dy and Cu–Dy interaction is found to be detrimental [16, 22, 39, 43, 44]. We further note that, unlike the two-component relaxation behavior reported previously [22], only the slow-relaxing component is recovered here, indicating that the near-zero-field regime is dominated exclusively by toroidal states.

2.5 | High-Field EPR Measurements

To investigate the low-energy electronic structure, we performed multifrequency high-field electron paramagnetic resonance (HF-EPR) spectroscopy on complexes **1** and **2**. The HF-EPR spectra of **2** at variable microwave frequencies up to 440 GHz and at a fixed temperature $T = 2$ K are shown in Figure 4a. Within the accessible magnetic field range, the spectra exhibit a single resonance feature consisting of a pronounced main absorption peak with a weaker shoulder on the low-field side. As the

15213773, 0, Downloaded from https://onlinelibrary.wiley.com/doi/10.1002/anie.7709103 by Rüdiger Klingeler - Universitatsbibliothek Heidelberg , Wiley Online Library on [06/11/2026]. See the Terms and Conditions (https://onlinelibrary.wiley.com/terms-and-conditions) on Wiley Online Library for rules of use; OA articles are governed by the applicable Creative Commons License

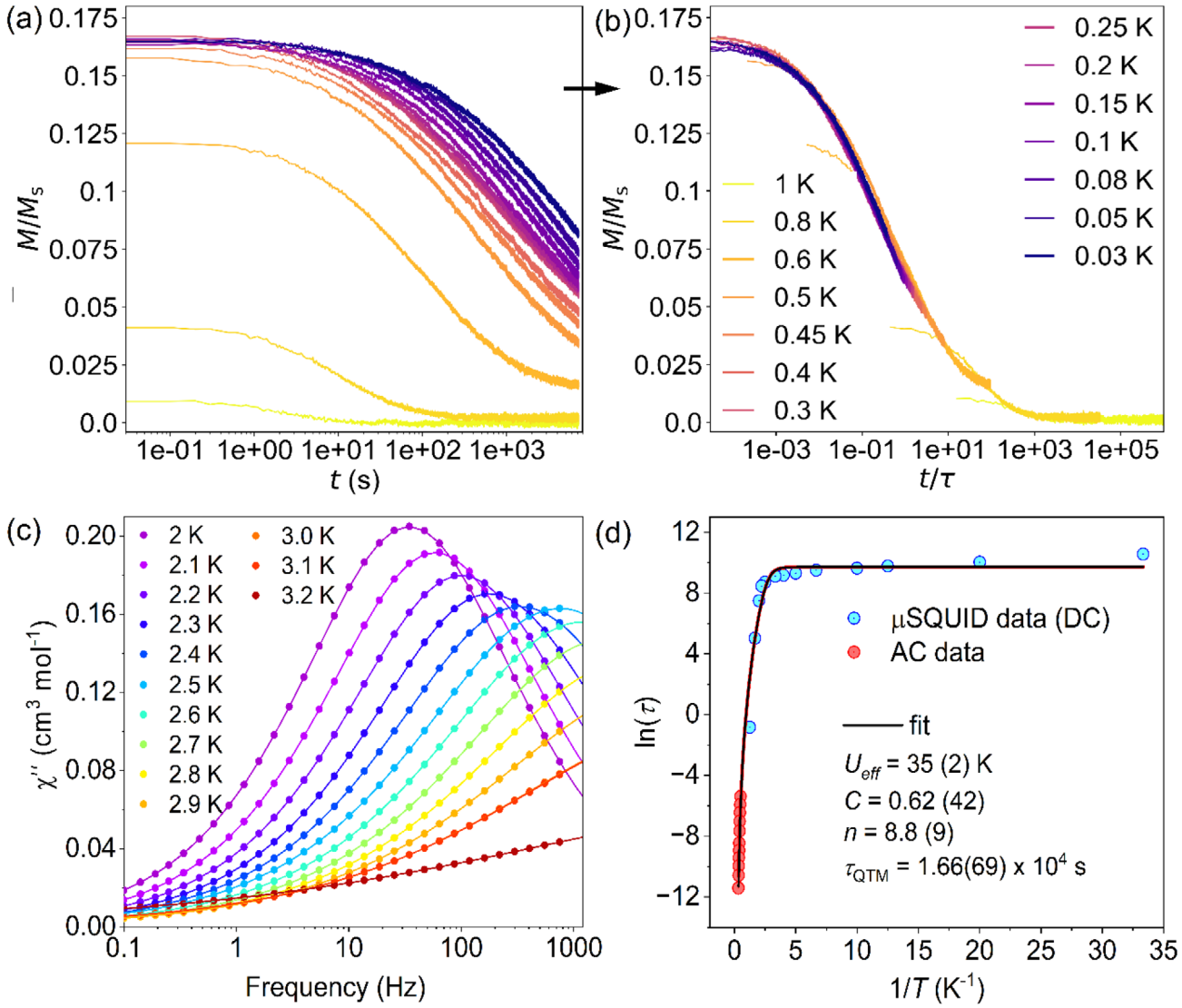


FIGURE 3 | Magnetization relaxation dynamics: (a) Magnetization relaxation measurements ($M(t)$) on single crystal of **1** obtained using μSQUIDs. Individual relaxation times are obtained by scaling to a master curve (b). (c) Frequency dependent AC susceptibility plots at various temperatures obtained by SQUID magnetometry on powder sample of **1**. (d) Combined logarithmic relaxation time ($\ln(\tau)$) versus $1/T$ data fitted to a generalized relaxation model.

excitation frequency increases, the resonance feature shifts to higher magnetic fields, and the separation between the main peak and its shoulder increases. Above 440 GHz, no resonance feature is discernible from the spectra in the accessible magnetic field range. At 260.5 GHz, the intensity of the pronounced main feature observed around 9 T remains almost constant when increasing the temperature up to 6 K and subsequently decreases upon heating in a Curie-like fashion (Figure S7). This temperature dependence indicates that the observed transition arises from (at least close to) the magnetic ground state at such high fields.

In contrast to the observation of low-energy magnetic excitations in **2**, the HF-EPR spectra of **1** at $T = 2$ K do not show any resonance feature at small microwave frequencies, that is, below a few hundred GHz. However, a broad absorption peak appears for $f > 440$ GHz, which shifts to higher magnetic fields with increasing excitation energy (Figure 4b). At the highest measured frequency of $f = 613.4$ GHz, a second broad resonance feature can be discerned at low magnetic fields. Combining the observed resonance features into a frequency-resonance-field diagram shows that the main high-field feature forms an almost linear resonance branch up to the highest measured fields and frequencies. The large widths of both resonance features suggest that they are likely composed of several magnetic transitions lying close in energy, for example, for different directions of the molecule with respect to the external magnetic field. The Curie-like decrease of the main feature's intensity with increasing temperature (Figure S8), furthermore, indicates that it is associated with an excitation from (at least energetically close to) the magnetic ground state.

2.6 | Theoretical Estimation of the Toroidal Ground State in Complex 1

The triangular geometry of the $\{Dy_3\}$ core in **1** provides a favorable structural framework for the emergence of a toroidal

15213773, 0, Downloaded from https://onlinelibrary.wiley.com/doi/10.1002/anie.7709103 by Rüdiger Klingeler - Universitatsbibliothek Heidelberg , Wiley Online Library on [06/11/2026]. See the Terms and Conditions (https://onlinelibrary.wiley.com/terms-and-conditions) on Wiley Online Library for rules of use; OA articles are governed by the applicable Creative Commons License

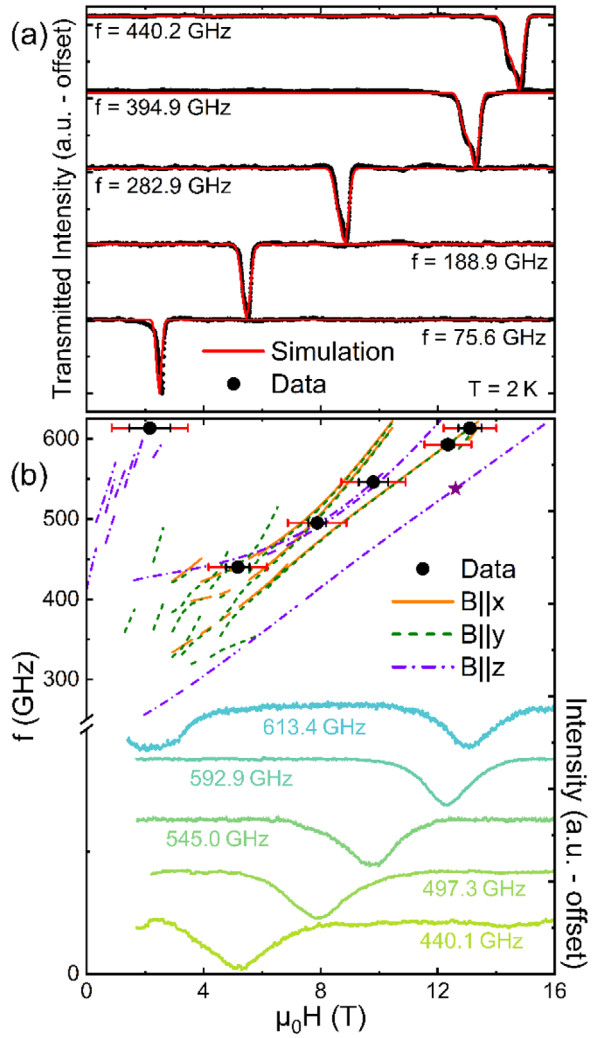


FIGURE 4 | (a) Experimental HF-EPR spectra of **2** (black) obtained at $T = 2$ K for various fixed frequencies. Red lines depict fits to the data as explained in the text. (b) Experimental HF-EPR spectra of **1** for various frequencies (right axis) and corresponding frequency-resonance-field diagram (left axis) obtained at $T = 2$ K. Black and red error bars mark the error margin in determining the resonance field and the FWHM, respectively. Lines depict simulations of the resonance branches with transition intensities of at least 10^{-4} of the most intense features, for different field directions, as described in the text. The asterisk marks a transition arising from a spin flip of one of the Dy(III) $s = 1/2$ pseudospins.

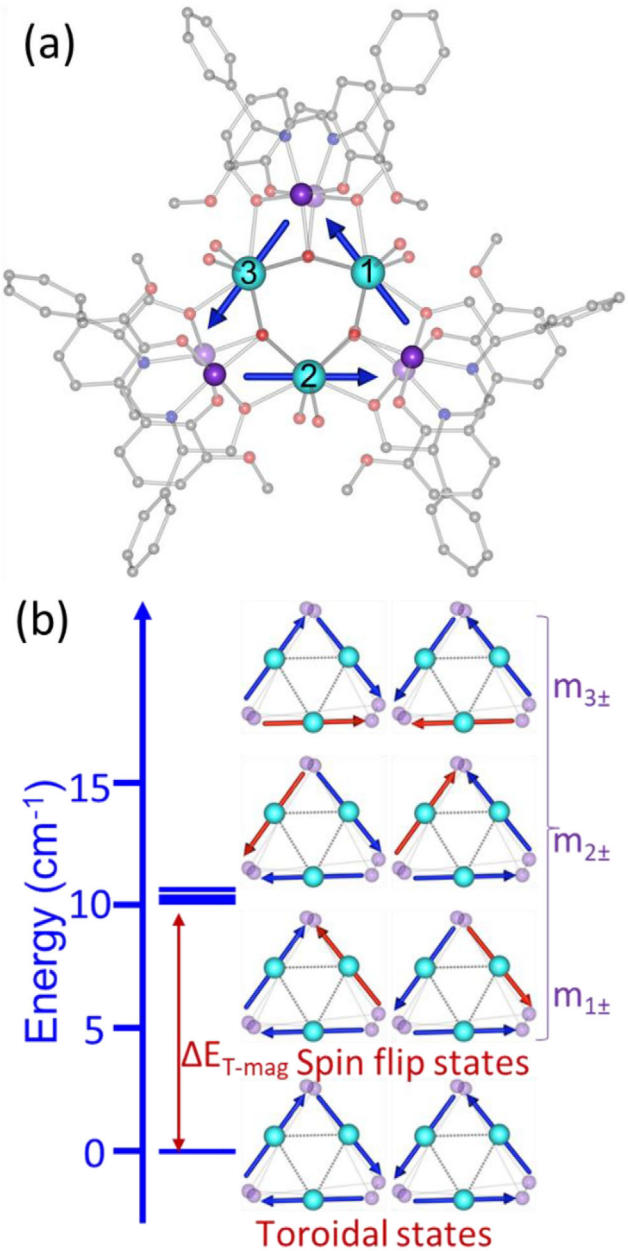


FIGURE 5 | (a) Orientation of the local magnetic anisotropy axes of each Dy(III) center in complex **1**. (b) Energy-level scheme of the exchange-coupled states with the corresponding magnetic moment configurations indicated by arrows.

ground state. To elucidate this assessment and to gain quantitative insight into the underlying electronic structure, ab initio CASSCF/RASSI-SO calculations, followed by SINGLE_ANISO analyses, were carried out using the MOLCAS 8.2 program package [45]. The single-ion magnetic anisotropies of the nine paramagnetic centers in complex **1**, comprising six Cu(II) and three Dy(III) ions, were evaluated. The ground-state Kramers doublets of all three Dy(III) centers display pronounced axial anisotropy, as evidenced by highly anisotropic g-tensors with negligibly small transverse components ($g_x \approx 0.004$, $g_y \approx 0.006$, and $g_z \approx 19.935$ for Dy1; $g_x \approx 0.022$, $g_y \approx 0.038$, and $g_z \approx 19.781$ for Dy2; $g_x \approx 0.005$, $g_y \approx 0.011$, and $g_z \approx 19.829$ for Dy3) (Table S6). This pronounced Ising-type behavior reflects the near-axial crystal-field environments imposed by the coordination geometry (Table S6). The calculated easy-axis orientations form a closed circular pattern within the $\{Dy_3\}$ core, unequivocally supporting a toroidal ground state (Figure 5a), which qualitatively explains the experimentally observed S-shaped magnetization curve of **1** (Figure 1b).

The computed tilting angle of the anisotropy axes with the $\{Dy_3\}$ plane ($\eta°$) is 8.8 ± 1.6, whereas the tilting angle with respect to the tangential direction ($\phi°$) is 9 ± 3 (Table S5 and Figure S9). Analysis of the crystal-field splitting reveals that the eight lowest Kramers doublets for Dy1, Dy2, and Dy3 span energy ranges of approximately 716, 621, and 668 cm^{-1}, respectively (Table S5). The ground-state wave functions are highly pure, being

15213773, 0, Downloaded from https://onlinelibrary.wiley.com/doi/10.1002/anie.7709103 by Rüdiger Klingeler - Universitätsbibliothek Heidelberg , Wiley Online Library on [06/11/2026]. See the Terms and Conditions (https://onlinelibrary.wiley.com/terms-and-conditions) on Wiley Online Library for rules of use; OA articles are governed by the applicable Creative Commons License

overwhelmingly dominated by the $|\pm 15/2\rangle$ component, further confirming the strong axial anisotropy of the Dy(III) centers and rationalizing the observed zero-field SMM behavior of complex **1**. Despite this, the presence of non-axial crystal-field contributions in the excited states introduces transverse terms into the effective spin Hamiltonian, which significantly enhances thermally-activated quantum tunnelling of magnetization (TA-QTM) at the single-ion level [46] (Table S6). Consequently, the calculated effective energy barriers for magnetization reversal, derived from the single-ion relaxation pathways, are 124 cm^{-1} (Dy1), 93 cm^{-1} (Dy2), and 115 cm^{-1} (Dy3) (Figure S10). These values are substantially higher than the experimentally observed effective energy barrier, indicating that the observed slow relaxation of complex **1** cannot be described solely by the single-ion anisotropy barriers of the individual Dy(III) centers (vide infra).

2.7 | Investigation of Magnetic Exchange Interactions

To rationalize the experimentally observed magnetic behavior, broken-symmetry density functional theory (BS-DFT) calculations were performed using the Gaussian 16 program suite to estimate the isotropic magnetic exchange interactions (see Computational Details in the Supporting Information). Direct evaluation of exchange parameters for the Dy(III) centers was not feasible within this framework. Therefore, calculations were carried out on the structurally analogous Y(III) complex (**2**). The diamagnetic Y(III) analogue enables reliable estimation of the Cu(II)–Cu(II) exchange interactions without complications arising from additional magnetic contributions. Based on the structural parameters, including coordination geometries, bond lengths, and angles, three distinct exchange pathways (J_1, J_2, and J_3) were identified for complex **2**. J_1 corresponds to the inter-triangular Cu–Cu exchange between adjacent Cu(II) sites of the two apical $\{Cu_3\}$ triangles, mediated by bridging ligands across the central $\{Y_3\}$ plane (highlighted as dotted green lines in Figure 6a). J_2 represents the intra-triangular Cu(II)–Cu(II) interactions within each $\{Cu_3\}$ unit, which are essential for inducing local triangular spin frustration (highlighted as dotted violet lines in Figure 6a). Finally, J_3 describes the inter-triangular Cu(II)–Cu(II) coupling between non-equivalent sites of the two $\{Cu_3\}$ triangles (highlighted as dotted lime-green lines in Figure 6a). The spin density is predominantly localized on the Cu(II) centers, with minor delocalization onto the bridging oxygen atoms and surrounding ligand framework, indicating that the magnetic exchange is primarily mediated through the oxygen bridges (Figure 6b).

Accordingly, the exchange Hamiltonian can be expressed as (Equation 1):

$$\begin{aligned}\mathcal{H}_{\mathrm{Cu-Cu}} = &-2J_1\left(\boldsymbol{S}_1\boldsymbol{S}_2 + \boldsymbol{S}_3\boldsymbol{S}_4 + \boldsymbol{S}_5\boldsymbol{S}_6\right)\\ &- 2J_2\left(\boldsymbol{S}_1\boldsymbol{S}_3 + \boldsymbol{S}_1\boldsymbol{S}_5 + \boldsymbol{S}_3\boldsymbol{S}_5 + \boldsymbol{S}_2\boldsymbol{S}_4 + \boldsymbol{S}_2\boldsymbol{S}_6 + \boldsymbol{S}_4\boldsymbol{S}_6\right)\\ &- 2J_3\left(\boldsymbol{S}_1\boldsymbol{S}_4 + \boldsymbol{S}_1\boldsymbol{S}_6 + \boldsymbol{S}_3\boldsymbol{S}_2 + \boldsymbol{S}_3\boldsymbol{S}_6 + \boldsymbol{S}_5\boldsymbol{S}_2 + \boldsymbol{S}_5\boldsymbol{S}_4\right) \quad (1)\end{aligned}$$

assuming purely isotropic Heisenberg exchange and $S_i = 1/2$. The above computed values $J_1^{\mathrm{DFT}} = -1.07$ cm^{-1}, $J_2^{\mathrm{DFT}} = -4.11$ cm^{-1}, and $J_3^{\mathrm{DFT}} = -0.67$ cm^{-1} suggest antiferromagnetic interactions

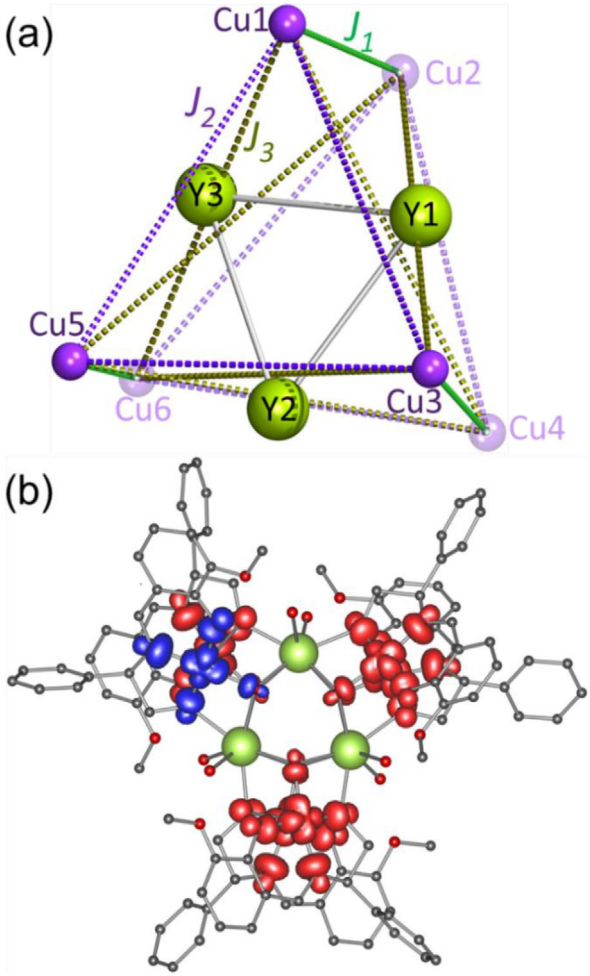


FIGURE 6 | (a) Schematic representation of the magnetic exchange pathways considered for the computational analysis for complex **2**, highlighting the distinct exchange interactions J_1 to J_3. (b) Spin density plot of the broken symmetry state calculated for the complex, where the red and blue isosurfaces represent positive (α) and negative (β) spin densities, respectively.

within and between the $\{Cu_3\}$ triangles. To enable quantitative correlation between theoretical predictions and experimentally observed magnetic behavior, the computed exchange parameters were subsequently used as starting parameters for fitting the measured magnetization and HF-EPR data.

The full spin Hamiltonian also needs to include the electronic Zeeman interaction and, thus, reads (Equation 2):

$$\mathcal{H}_{2-\mathrm{Y}} = \sum_{i=1}^{6} \mu_{\mathrm{B}} \boldsymbol{B} \overleftrightarrow{R}_i(\theta_i, \varphi)\, \overleftrightarrow{g}\, \overleftrightarrow{R}_i^{T}(\theta_i, \varphi)\, \boldsymbol{S}_i + \mathcal{H}_{\mathrm{Cu-Cu}} \quad (2)$$

assuming an axial g-tensor $\overleftrightarrow{g}$ = ($g_\perp$, $g_\perp$, and $g_\parallel$) whose orientation within the molecular frame is given by the rotation matrix $\overleftrightarrow{R}_i(\theta_i, \varphi)$. $\mathcal{H}_{\mathrm{Cu-Cu}}$ is the exchange interaction between the Cu(II) moments as described in Equation (1). The relative angles between the g-tensors within the Cu_3-plane, θ_i, are fixed to multiples of 120° within each $\{Cu_3\}$ triangle and to 36° between inter-triangular adjacent Cu(II) sites, as given by the

15213773, 0, Downloaded from https://onlinelibrary.wiley.com/doi/10.1002/anie.7709103 by Rüdiger Klingeler - Universitatsbibliothek Heidelberg , Wiley Online Library on [06/11/2026]. See the Terms and Conditions (https://onlinelibrary.wiley.com/terms-and-conditions) on Wiley Online Library for rules of use; OA articles are governed by the applicable Creative Commons License

pseudo-trigonal molecular symmetry, while the out-of-plane angle φ needs to be taken as a free fit parameter. The best fit to the experimental data is achieved by $g_\perp = 2.08(2)$, $g_\parallel = 2.26(1)$, $\varphi = 35(7)°$, $J_1^{exp} = -1.5(2)$ cm^{-1}, $J_2^{exp} = -3.4(3)$ cm^{-1}, and $J_3^{exp} = -0.46(11)$ cm^{-1} and shown as solid lines in Figures 1b, 4a, and S11. The obtained *g*-tensor is typical for Cu(II) ions in octahedral ligand fields [47, 48], and its magnitude and orientation are in qualitative agreement with our theoretical calculations (Figure S12). Similarly, the extracted exchange coupling parameters confirm antiferromagnetic intra- and inter-triangular interaction as predicted by BS-DFT. Given the approximation of equilateral isotropic magnetic coupling, the dominant (J_2) interaction leads to spin frustration within the {Cu_3} triangles, resulting in a doubly degenerate doublet ground state. The presence of two such triangles in the crystal structure gives rise to a fourfold-degenerate doublet manifold. The weaker J_1 and J_3, then, couple these units to a diamagnetic $S = 0$ ground state, which persists up to $B = 2$ T, as shown in the simulated Zeeman diagram with the magnetic field applied parallel to the *x*-axis (Figure S13)

Having established the nature of the exchange-coupled ground state in complex **2**, we next turned our attention to complex **1** to elucidate the collective magnetic properties and the possible emergence of toroidal states within the exchange-coupled system. The effects of exchange and dipolar interactions on the stabilization of the low-lying energy states were investigated using the Lines model implemented in the POLY_ANISO program. Owing to the large size of the system and the resulting number of exchange-coupled states exceeding the computational limits of POLY_ANISO, the magnetic model was simplified by considering antiferromagnetic coupling within each {Cu_3} triangle, as established for complex **2**, thereby reducing each triangular unit to an effective $S = 1/2$. This approximation allows the magnetic behavior of the system to be modelled using an effective {Cu_2Dy_3} framework for the exchange-coupled state. Powder magnetic susceptibility and magnetization data for complex **1** were then fit, yielding best-fit parameters summarized in Table S7; Figures 1b and S3. Since the first excited crystal-field states of all three Dy(III) centers lie well above the estimated exchange energies (> 90 cm^{-1}), only the ground Kramers doublets were considered in constructing the Zeeman energy diagram. The resulting Zeeman spectrum with the magnetic field applied parallel to the *x*-axis (Figure S14) illustrates the evolution of the lowest exchange-coupled states under an applied magnetic field. The ground state can be described by the toroidal states $|T_{z\pm}\rangle = |\pm1,\pm1,\pm1\rangle$, corresponding to clockwise and counterclockwise arrangements of the Dy(III) magnetic moments; the two components $|T_{z+}\rangle$ and $|T_{z-}\rangle$ constitute a doubly degenerate toroidal ground state related to each other by time-reversal symmetry. Owing to the slight out-of-plane canting of the local anisotropy axes, a small residual magnetic moment is present, rendering the ground state nearly nonmagnetic rather than strictly silent (Figure 5b). Notably, the absence of level crossings up to ≈ 1.3 T confirms toroidal blocking and demonstrates qualitative agreement between the computed exchange parameters, ab initio energies, and the experimentally observed switching field (vide infra).

However, despite successfully capturing the general magnetic behavior, the simplified {Cu_2Dy_3} model reproduces the experimental M versus H behavior only qualitatively (Figure S3), highlighting the limitations associated with reducing the full {Cu_6Dy_3} cluster to an effective spin framework. This observation suggests that the Cu(II)–Dy(III) exchange interactions play a more significant role in governing the overall magnetic response of the cluster than accounted for within the simplified POLY_ANISO treatment. Therefore, to gain deeper insight into the exchange-coupled ground state, an alternative effective spin-Hamiltonian approach was considered. Given that the Dy(III) magnetic ground state corresponds to a well-isolated and nearly perfectly axial $m_j = \pm 15/2$ Kramers doublet, the Dy(III) magnetic moments can be treated as Ising spins at sufficiently low temperatures. The resulting POLY_ANISO calculations yield low-lying exchange-coupled states with an effective barrier of approximately (U_{cal}) ~30 cm^{-1}, substantially closer to U_{eff} than the single-ion barriers. Consequently, both Dy(III)–Dy(III) and Cu(II)–Dy(III) interactions may be approximated within an Ising-like formalism, allowing the magnetic behavior of the system to be described using the effective Hamiltonian shown in Equation (3):

$$\mathcal{H}_{1-\mathbf{Dy}} = \mathcal{H}_{2-\mathbf{Y}} + \sum_{j=1}^{3} \mu_B \boldsymbol{B} \overleftrightarrow{g}_{Dy} \boldsymbol{s_j} + 15 \sum_{\langle i,j \rangle} -2J_{Cu-Dy} S_i^z s_j^z + 225 \sum_{j,k=1,\ j<k}^{3} -2J_{Dy-Dy} s_j^z s_{j+1}^z \quad (3)$$

when presuming the transferability of the spin Hamiltonian parameters from **2**. Here, $\boldsymbol{s}_j$ is the Dy(III) pseudospin with pseudospin $s = 1/2$ resulting from its Ising-like character and $\boldsymbol{s}_j^z$ and $\boldsymbol{S}_i^z$ denote the projection of this pseudospin and of the Cu(II) moments along the corresponding local (site *j*) Dy(III) anisotropy axis, respectively. The second sum couples the Dy(III) moments with the four nearest Cu(II) sites, respectively. Using this Hamiltonian, we performed simulations of the low-temperature magnetization and HF-EPR data (vide infra), employing the *g*-tensor values and orientations obtained from the SINLE_ANISO calculations, which leaves only the magnetic coupling constants as free parameters. This, however, did not yield a satisfactory description of the experimental results (Figure 7b). To achieve a good agreement of simulation and experiment, the tilting angle of each Dy(III) anisotropy axis out of the {Dy_3} plane was set to 16°. Similarly, large changes of the in-plane angles were found to not significantly alter the simulations (Figure 7b). The discrepancy of a few degrees in the g-tensor orientation to the predictions of the SINGLE_ANISO calculations is not uncommon for lanthanide ions in organic ligand coordination [49–52], and might additionally arise due to the presence of a sizable Cu(II)–Dy(III) and Dy(III)–Dy(III) coupling in the here reported case. With this approach the best simulation results were obtained by $J_{Cu-Dy} = 0.40(3)$ cm^{-1} and $J_{Dy-Dy} = 0.028(2)$ cm^{-1} and are shown in Figures 7a, S15, and 4b for the magnetization and f-B-diagram, respectively. As predicted earlier, our simulations of the transition energies (Figure 4b) reveal that the observed broad resonance feature in the HF-EPR spectra of **1** is attributed to a bunch of energetically close-lying transitions. Additionally, the simulations predict another resonance at higher magnetic fields, marked by an asterisk in Figure 4b, which mainly corresponds to a spin flip of one of the Dy(III) pseudospins. Such a transition is, however, highly symmetry-forbidden when considering the actual angular momentum of $J = 15/2$, and, thus, not observed in the experiment.

15213773, 0, Downloaded from https://onlinelibrary.wiley.com/doi/10.1002/anie.7709103 by Rüdiger Klingeler - Universitatsbibliothek Heidelberg , Wiley Online Library on [06/11/2026]. See the Terms and Conditions (https://onlinelibrary.wiley.com/terms-and-conditions) on Wiley Online Library for rules of use; OA articles are governed by the applicable Creative Commons License

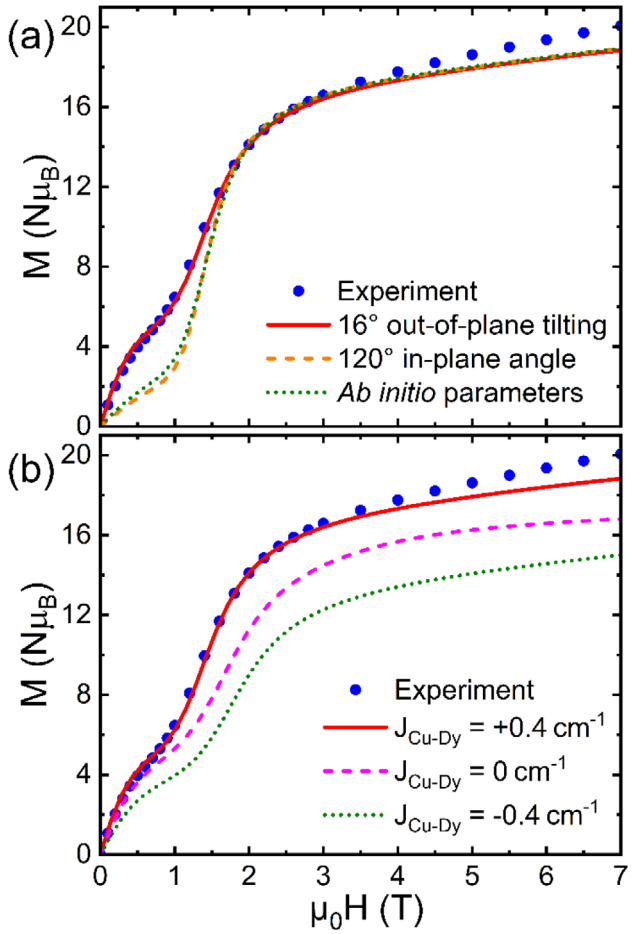


FIGURE 7 | Experimental and simulated field-dependent powder magnetization curves for complex **1**. (a) Simulations considering different orientations of the local Dy(III) anisotropy. (b) Simulations assuming different $J_{Cu\text{-}}$ exchange coupling parameters. Blue symbols represent the experimental data, while lines correspond to the calculated simulations as described in the text.

3 | Discussion

The observed large toroidal blocking field of complex **1** is a direct consequence of the microscopic magnetic interactions as determined by our analysis of the experimental data. In typical $\{Dy_3\}$ triangular SMTs, the primary contribution to $\mu_0 H_C$ is J_{Dy-Dy}, which arises from a combination of the magnetic exchange and dipolar interactions between the lowest Kramers doublets on the Dy(III) sites. Here, the obtained effective Dy(III)–Dy(III) coupling constant is found to be ferromagnetic, which can be understood as the projection of an antiferromagnetic interaction ($J^{Lines}_{Dy-Dy} = J_{Dy-Dy}/25cos\ (120°) = -2.2 \cdot 10^{-4}$ cm^{-1}) between the Dy(III) moments on the local pseudospin frame [17]. In particular, J_{Dy-Dy} of complex **1** exceeds the values reported for other Dy_3(III)-based SMTs with the hitherto highest blocking fields of up to 0.8 T [14, 17]. Since the Dy-Dy distances do not significantly differ between the molecules, it seems reasonable to attribute the enhancement of J_{Dy-Dy} in complex **1** to a stronger contribution of magnetic exchange. It has been found recently that changes in the Dy(III)–Dy(III) bond geometry can significantly alter the ratio of dipolar and exchange contributions to the overall magnetic coupling [18]. However, the relevant bond angles in complex **1** are only slightly different from those reported in other SMTs. Hence, we propose that J_{Dy-Dy} may be increased by the presence of the Cu(II) ion orbitals in the adjacent $\{Cu_3\}$ triangles offering an additional pathway for electronic exchange.

The ferromagnetic nature of the Cu(II)–Dy(III) interaction J_{Cu-Dy} is well understood in the frame of magnetic exchange via a virtual 3d→5d charge transfer state [47, 53, 54], as proposed independently by Kahn et al. [55] and Gatteschi and coworkers [56, 57]. Our analysis shows that the central toroidal $\{Dy_3\}$ unit exhibits an effective exchange bias through the magnetic interaction to the adjacent spin-frustrated $\{Cu_3\}$ triangles. To investigate the role of this exchange bias, we performed simulations of the low temperature magnetization for the case of non-interacting ($J_{Cu-Dy} = 0$) and antiferromagnetically coupled ($J_{Cu-Dy} = -0.40$ cm^{-1}) Cu(II) and Dy(III) ions. The obtained $M(H)$ and $\partial M/\partial H(H)$ curves are shown in Figures 7a and S16, respectively. Our simulations clearly demonstrate that the ferromagnetic exchange bias present in complex **1** destabilizes the toroidal ground state as the resulting blocking field decreases compared to the non-interacting scenario. Moreover, our results suggest that an antiferromagnetic 3d–4f exchange is preferable to increase the toroidal blocking field even further. From a synthetic point of view, this could, in principle, be achieved by substituting the Cu(II) sites with 3d transition metal ions with partially occupied t_{2g} orbitals, favoring a 3d→4f charge transfer process, such as Cr(III)/(IV) or V(III)/(IV) [54, 58]. However, it should be noted that the presence of Cu(II) ions in complex **1** might not only lead to an exchange bias effect through their magnetic coupling to the central Dy(III) moments, but, as discussed earlier, may also give rise to an additional electronic pathway affecting the Dy(III)–Dy(III) exchange interaction, and thereby leading to the observed enhancement of J_{Dy-Dy}.

Taken together, the unusually large toroidal blocking field in complex **1** is primarily governed by the enhanced effective Dy(III)–Dy(III) interaction, which should be distinguished from the direct Cu(II)–Dy(III) exchange. A possible contribution to this enhancement may arise from Cu-induced modification of the bridging-ligand electronic structure and, consequently, the Dy–Dy exchange pathway. This is supported by further analysis wherein J_{Dy-Dy} and J_{Cu-Dy} were varied independently to simulate the magnetization data, which shows that J_{Dy-Dy} primarily determines the field scale of the toroidal-to-spin-flip transition, whereas the ferromagnetic J_{Cu-Dy}interaction destabilizes the toroidal state. Thus, the Cu-containing framework may introduce two counteracting effects, whose combined influence determines the observed toroidal blocking field (Figure S17).

4 | Conclusions

In summary, our experimental and computational results suggest an effective and chemically accessible route to stabilizing toroidal magnetization against high magnetic fields. Through the synthesis and comprehensive magnetic characterization of a heterometallic {3d–4f} family, we show that the Dy-containing complex exhibits a magnetically silent toroidal ground state that remains robust up to switching fields exceeding 1.3 T, far surpassing previously reported single-molecule toroids. This unprecedented enhancement is shown to result from a strong

15213773, 0, Downloaded from https://onlinelibrary.wiley.com/doi/10.1002/anie.7709103 by Rüdiger Klingeler - Universitatsbibliothek Heidelberg , Wiley Online Library on [06/11/2026]. See the Terms and Conditions (https://onlinelibrary.wiley.com/terms-and-conditions) on Wiley Online Library for rules of use; OA articles are governed by the applicable Creative Commons License

magnetic Dy(III)–Dy(III) exchange interaction protecting the circulating $\{Dy_3\}$ moment against the external magnetic field. The microscopic origin of such an enhanced Dy(III)–Dy(III) coupling remains elusive but may arise due to the presence of the adjacent Cu(II) orbitals. However, our analysis also reveals that the exchange-active, spin-frustrated $\{Cu_3\}$ triangular units generate an internal ferromagnetic bias field that destabilizes the toroidal ground state. While the blocking temperature remains limited by relaxation via the low-lying exchange-coupled states rather than by the intrinsic single-ion anisotropy barrier, the dramatic increase in the toroidal blocking field reported here suggests new design principles for field-resilient single-molecule toroids and opens promising avenues toward electrically addressable, low-noise molecular magnetic units for quantum, spintronic, and magnetoelectric applications.

Author Contributions

Deepanshu Chauhan: conceptualization, investigation, methodology, validation, visualization, software, formal analysis, data curation, writing – review and editing, and writing – original draft. **Jan Arneth**: conceptualization, methodology, software, data curation, formal analysis, validation, writing – original draft, and writing – review and editing. **Sagar Paul**: conceptualization, methodology, software, data curation, supervision, formal analysis, resources, visualization, writing – review and editing, and writing – original draft. **Bapan Jana**: conceptualization, methodology, writing – original draft, and writing – review and editing. **Wolfgang Wernsdorfer**: conceptualization, methodology, software, data curation, supervision, resources, project administration, writing – review and editing, and writing – original draft. **Rüdiger Klingeler**: conceptualization, methodology, software, data curation, project administration, writing – review and editing, and writing – original draft. **Maheswaran Shanmugam**: conceptualization, methodology, validation, resources, writing – review and editing, writing – original draft, and visualization. **Gopalan Rajaraman**: conceptualization, writing – review and editing, writing – original draft, funding acquisition, visualization, project administration, resources, and supervision.

Acknowledgments

G.R. acknowledges funding support from the National Quantum Mission (DST/QTC/NQM/QMD/2024/4), an initiative of the Department of Science and Technology, Government of India. M.S. thanks the funding agencies SERB (CRG/2023/002178), BRNS (58/14/07/2023-BRNS/37029), CSIR (01/3092/23/EMR-II), IISc-STARs (MoE-STARS/STARS-2/2023-0158), and IIT Bombay for the financial support. S.P. and W.W. thank the German Research Foundation (DFG) for the Gottfried Wilhelm Leibniz-Award, ZVN-2020_WE 4458-5 and DFG-CCR 1573 "4f for future" (project B4) for support.

Conflicts of Interest

The authors declare no conflicts of interest.

Data Availability Statement

The data that supports the findings of this study are available in the Supporting Information of this article.

References

1. E. Moreno-Pineda and W. Wernsdorfer, "Measuring Molecular Magnets for Quantum Technologies," *Nature Reviews Physics* 3 (2021): 645–659, https://doi.org/10.1038/s42254-021-00340-3.

2. M. R. Wasielewski, M. D. E. Forbes, N. L. Frank, et al., "Exploiting Chemistry and Molecular Systems for Quantum Information Science," *Nature Reviews Chemistry* 4 (2020): 490–504, https://doi.org/10.1038/s41570-020-0200-5.

3. A. Gaita-Ariño, F. Luis, S. Hill, and E. Coronado, "Molecular Spins for Quantum Computation," *Nature Chemistry* 11 (2019): 301–309, https://doi.org/10.1038/s41557-019-0232-y.

4. C. A. Gould, K. R. Mcclain, D. Reta, et al., "Ultrahard Magnetism From Mixed-Valence Dilanthanide Complexes With Metal-Metal Bonding," *Science* 375 (2022): 198–202, https://doi.org/10.1126/science.abl5470.

5. J. Emerson-King, G. K. Gransbury, B. E. Atkinson, et al., "Soft Magnetic Hysteresis in a Dysprosium Amide–alkene Complex up to 100 Kelvin," *Nature* 643 (2025): 125–129, https://doi.org/10.1038/s41586-025-09138-0.

6. C. A. Goodwin, F. Ortu, D. Reta, N. F. Chilton, and D. P. Mills, "Molecular Magnetic Hysteresis at 60 Kelvin in Dysprosocenium," *Nature* 548 (2017): 439–442, https://doi.org/10.1038/nature23447.

7. L. Bogani and W. Wernsdorfer, "Molecular Spintronics Using Single-Molecule Magnets," *Nature Materials* 7 (2008): 179–186, https://doi.org/10.1038/nmat2133.

8. D. N. Woodruff, R. E. Winpenny, and R. A. Layfield, "Lanthanide Single-Molecule Magnets," *Chemical Reviews* 113 (2013): 5110–5148, https://doi.org/10.1021/cr400018q.

9. J. Tang and P. Zhang, *Lanthanide Single Molecule Magnets*, Vol. 2 (Springer, 2015), https://doi.org/10.1007/978-3-662-46999-6.

10. Z. Zhu, M. Guo, X.-L. Li, and J. Tang, "Molecular Magnetism of Lanthanide: Advances and Perspectives," *Coordination Chemistry Reviews* 378 (2019): 350–364, https://doi.org/10.1016/j.ccr.2017.10.030.

11. D. Chauhan, D. Saini, D. Borah, et al., "Room Temperature Giant Magnetoelectric Coupling in $\{Co^{III}_3\ Dy^{III}\}$ Molecular Single Crystal Derived Nanogenerator," *Journal of the American Chemical Society* 148 (2026): 11738–11748, https://doi.org/10.1021/jacs.5c20429.

12. B. B. Van Aken, J.-P. Rivera, H. Schmid, and M. Fiebig, "Observation of Ferrotoroidic Domains," *Nature* 449 (2007): 702–705.

13. L. Ding, X. Xu, H. O. Jeschke, et al., "Field-Tunable Toroidal Moment in a Chiral-Lattice Magnet," *Nature Communications* 12 (2021): 5339, https://doi.org/10.1038/s41467-021-25657-6.

14. Z. Zhu, X. Ying, L. C. Adi, et al., "Homochiral Toroidal Spin state in Dy(III)-Based Single-Molecule Toroics," *Nature Chemistry* 18 (2026): 1004–1013.

15. S. MüHlbauer, B. Binz, F. Jonietz, et al., "Skyrmion Lattice in a Chiral Magnet," *Science* 323 (2009): 915–919, https://doi.org/10.1126/science.1166767.

16. J. Tang, I. Hewitt, N. Madhu, et al., "Dysprosium Triangles Showing Single-Molecule Magnet Behavior of Thermally Excited Spin States," *Angewandte Chemie International Edition* 45 (2006): 1729–1733, https://doi.org/10.1002/anie.200503564.

17. L. Chibotaru, L. Ungur, and A. Soncini, "The Origin of Nonmagnetic Kramers Doublets in the Ground State of Dysprosium Triangles: Evidence for a Toroidal Magnetic Moment," *Angewandte Chemie International Edition* 47 (2008): 4126–4129, https://doi.org/10.1002/anie.200800283.

18. K. R. Vignesh and G. Rajaraman, "Strategies to Design Single-Molecule Toroics Using Triangular $\{Ln_3\}$ n Motifs," *ACS Omega* 6 (2021): 32349–32364, https://doi.org/10.1021/acsomega.1c05310.

19. N. Talebi, S. Guo, and P. A. van Aken, "Theory and Applications of Toroidal Moments in Electrodynamics: Their Emergence, Characteristics, and Technological Relevance," *Nanophotonics* 7 (2018): 93–110, https://doi.org/10.1515/nanoph-2017-0017.

20. X.-L. Li and J. Tang, "Recent Developments in Single-Molecule Toroics," *Dalton Transactions* 48 (2019): 15358–15370, https://doi.org/10.1039/C9DT02113B.

15213773, 0, Downloaded from https://onlinelibrary.wiley.com/doi/10.1002/anie.7709103 by Rüdiger Klingeler - Universitatsbibliothek Heidelberg , Wiley Online Library on [06/11/2026]. See the Terms and Conditions (https://onlinelibrary.wiley.com/terms-and-conditions) on Wiley Online Library for rules of use; OA articles are governed by the applicable Creative Commons License

21. X. L. Li, Z. Ma, and J. Tang, "Recent Developments of Nontraditional Single-Molecule Toroics," *Chemistry: A European Journal* 30 (2024): e202304369.

22. D. Chauhan, S. Paul, D. Borah, et al., "Ultraslow Relaxation of Toroidal State in Ferrotoroidal Dysprosium Complex," *Journal of the American Chemical Society* 147 (2025): 39572–39581, https://doi.org/10.1021/jacs.5c12742.

23. H. Kaemmerer, A. Baniodeh, Y. Peng, et al., "Inorganic Approach to Stabilizing Nanoscale Toroidicity in a Tetraicosanuclear $Fe_{18}Dy_6$ Single Molecule Magnet," *Journal of the American Chemical Society* 142 (2020): 14838–14842, https://doi.org/10.1021/jacs.0c07168.

24. K. R. Vignesh, A. Soncini, S. K. Langley, W. Wernsdorfer, K. S. Murray, and G. Rajaraman, "Ferrotoroidic Ground state in a Heterometallic $\{Cr^{III}Dy^{III}{}_6\}$ Complex Displaying Slow Magnetic Relaxation," *Nature Communications* 8 (2017): 1023, https://doi.org/10.1038/s41467-017-01102-5.

25. M. Gysler, F. El Hallak, L. Ungur, et al., "Multitechnique Investigation of Dy_3 – implications for Coupled Lanthanide Clusters," *Chemical Science* 7 (2016): 4347–4354, https://doi.org/10.1039/C6SC00318D.

26. Y. Peng, J. Braun, L. Scherthan, et al., "Adding 161Dy-Mössbauer Spectroscopy to a Multitechnique Investigation of Magnetic Transitions in a $\{Co^{III}{}_3Dy^{III}{}_3\}$ Single-Molecule Toroic," *Nature Communications* 17 (2026): 3864, https://doi.org/10.1038/s41467-026-71058-y.

27. G. Fernandez Garcia, D. Guettas, V. Montigaud, et al., "A Dy_4 Cubane: A New Member in the Single-Molecule Toroics Family," *Angewandte Chemie International Edition* 130 (2018): 17335–17339, https://doi.org/10.1002/ange.201810156.

28. J. Wu, X.-L. Li, M. Guo, L. Zhao, Y.-Q. Zhang, and J. Tang, "Realization of Toroidal Magnetic Moments in Heterometallic 3d–4f Metallocycles," *Chemical Communications* 54 (2018): 1065–1068, https://doi.org/10.1039/C7CC09391H.

29. P.-H. Guo, J.-L. Liu, Z.-M. Zhang, et al., "The First $\{Dy_4\}$ Single-Molecule Magnet With a Toroidal Magnetic Moment in the Ground State," *Inorganic Chemistry* 51 (2012): 1233–1235, https://doi.org/10.1021/ic202650f.

30. G. Novitchi, G. Pilet, L. Ungur, et al., "Heterometallic Cu^{II}/Dy^{III} 1D Chiral Polymers: Chirogenesis and Exchange Coupling of Toroidal Moments in Trinuclear Dy_3 Single Molecule Magnets," *Chemical Science* 3 (2012): 1169, https://doi.org/10.1039/c2sc00728b.

31. D. Chauhan, R. K. Tiwari, and G. Rajaraman, "Surface Stabilization to Enhance Single Molecule Toroidal Behavior in $\{Dy_3\}$ Molecules: The Impact of Au(111), MgO, and Graphene Surfaces," *Small* 21 (2025): 2412283, https://doi.org/10.1002/smll.202412283.

32. S. Mondal, D. Chauhan, T. Guizouarn, et al., "Self-Assembled Lanthanide Phosphinate Square Grids (Ln = Er, Dy, and Tb): Dy_4 Shows SMM/SMT and Tb_4 SMT Behavior," *Inorganic Chemistry* 63 (2024): 22338–22348, https://doi.org/10.1021/acs.inorgchem.4c02567.

33. Z. Zhu, X. Ying, L. C. Adi, et al., "Homochiral Toroidal Spin state in Dy(III)-Based Single-Molecule Toroics," *Nature Chemistry* 18 (2026): 1004–1013, https://doi.org/10.1038/s41557-026-02070-4.

34. L. Ungur, S. K. Langley, T. N. Hooper, et al., "Net Toroidal Magnetic Moment in the Ground State of a $\{Dy_6\}$-Triethanolamine Ring," *Journal of the American Chemical Society* 134 (2012): 18554–18557, https://doi.org/10.1021/ja309211d.

35. Y.-C. Chen and M.-L. Tong, "Single-Molecule Magnets Beyond a Single Lanthanide Ion: The Art of Coupling," *Chemical Science* 13 (2022): 8716–8726, https://doi.org/10.1039/D2SC01532C.

36. A. Swain, T. Sharma, and G. Rajaraman, "Strategies to Quench Quantum Tunneling of Magnetization in Lanthanide Single Molecule Magnets," *Chemical Communications* 59 (2023): 3206–3228, https://doi.org/10.1039/D2CC06041H.

37. D. Chauhan, K. R. Vignesh, A. Swain, et al., "Exploiting Strong $\{Cr^{III}$–$Dy^{III}\}$ Ferromagnetic Exchange Coupling to Quench Quantum Tunneling of Magnetization in a Novel $\{Cr^{III}{}_2\ Dy^{III}{}_3\}$ Single-Molecule Magnet," *Crystal Growth & Design* 23 (2022): 197–206, https://doi.org/10.1021/acs.cgd.2c00888.

38. C. Y. Chow, H. Bolvin, V. E. Campbell, et al., "Assessing the Exchange Coupling in Binuclear Lanthanide(iii) Complexes and the Slow Relaxation of the Magnetization in the Antiferromagnetically Coupled Dy 2 Derivative," *Chemical Science* 6 (2015): 4148–4159, https://doi.org/10.1039/C5SC01029B.

39. Z. Zhu, S. Paul, C. Zhao, et al., "Record Quantum Tunneling Time in an Air-Stable Exchange-Bias Dysprosium Macrocycle," *Journal of the American Chemical Society* 146 (2024): 18899–18904, https://doi.org/10.1021/jacs.4c07412.

40. J. D. Rinehart, M. Fang, W. J. Evans, and J. R. Long, "AN $_2{}^{3-}$ Radical-Bridged Terbium Complex Exhibiting Magnetic Hysteresis at 14 K," *Journal of the American Chemical Society* 133 (2011): 14236–14239, https://doi.org/10.1021/ja206286h.

41. J. D. Rinehart and J. R. Long, "Exploiting Single-Ion Anisotropy in the Design of f-Element Single-Molecule Magnets," *Chemical Science* 2 (2011): 2078, https://doi.org/10.1039/c1sc00513h.

42. S. Paul, G. Kotagiri, R. Ganguly, et al., "Magnetization Reversal Across Multiple Serial Barriers in a Single Fe_3O_4 Nanoparticle," *Physical Review B* 105 (2022): L180410, https://doi.org/10.1103/PhysRevB.105.L180410.

43. S. Y. Lin, W. Wernsdorfer, L. Ungur, et al., "Coupling Dy 3 Triangles to Maximize the Toroidal Moment," *Angewandte Chemie International Edition* 51 (2012): 12767–12771, https://doi.org/10.1002/anie.201206602.

44. J. Goura, E. Colacio, J. M. Herrera, et al., "Heterometallic Zn_3Ln_3 Ensembles Containing (μ_6-CO_3) Ligand and Triangular Disposition of Ln 3^+ Ions: Analysis of Single-Molecule Toroic (SMT) and Single-Molecule Magnet (SMM) Behavior," *Chemistry: A European Journal* 23 (2017): 16621–16636, https://doi.org/10.1002/chem.201703842.

45. F. Aquilante, J. Autschbach, R. K. Carlson, et al., "Molcas 8: New Capabilities for Multiconfigurational Quantum Chemical Calculations Across the Periodic Table," *Journal of Computational Chemistry* 37 (2016): 506–541, https://doi.org/10.1002/jcc.24221.

46. J. Arneth, L. Spillecke, C. Koo, T. A. Bazhenova, E. B. Yagubskii, and R. Klingeler, "The Relevance of Non-Axiality and Low-Lying Excited States for Slow Magnetic Relaxation in Pentagonal-Bipyramidal Erbium(III) Complexes Probed by High-Frequency EPR," *Chemistry: A European Journal* 31 (2025): e202500369, https://doi.org/10.1002/chem.202500369.

47. N. Ahmed, T. Sharma, L. Spillecke, et al., "Probing the Origin of Ferro-/Antiferromagnetic Exchange Interactions in Cu(II)–4f Complexes," *Inorganic Chemistry* 61 (2022): 5572–5587, https://doi.org/10.1021/acs.inorgchem.2c00065.

48. C. Koo, J. Park, J. Butscher, E. Rentschler, and R. Klingeler, "High-Frequency EPR Study on Cu_4Cu- and Co_4Co-Metallacrown Complexes," *Journal of Magnetism and Magnetic Materials* 477 (2019): 340–343, https://doi.org/10.1016/j.jmmm.2019.01.038.

49. Y. S. Meng, J. Xiong, M. W. Yang, et al., "Experimental Determination of Magnetic Anisotropy in Exchange-Bias Dysprosium Metallocene Single-Molecule Magnets," *Angewandte Chemie International Edition* 132 (2020): 13137–13143, https://doi.org/10.1002/ange.202004537.

50. K. Bernot, J. Luzon, L. Bogani, et al., "Magnetic Anisotropy of Dysprosium(III) in a Low-Symmetry Environment: A Theoretical and Experimental Investigation," *Journal of the American Chemical Society* 131 (2009): 5573–5579, https://doi.org/10.1021/ja8100038.

51. J. S. Carneiro Neto, G. K. Gransbury, L. G. Fachini, et al., "Balance Between Crystal Field and Phonon Optimization in Defining the Magnetic Properties of Lanthanide Dichalcogenoimidodiphosphinate Complexes," *Inorganic Chemistry* 64 (2025): 21879–21892, https://doi.org/10.1021/acs.inorgchem.5c03025.

52. E. Lucaccini, M. Briganti, M. Perfetti, et al., "Relaxation Dynamics and Magnetic Anisotropy in a Low-Symmetry Dy III Complex," *Chemistry: A European Journal* 22 (2016): 5552–5562, https://doi.org/10.1002/chem.201505211.

15213773, 0, Downloaded from https://onlinelibrary.wiley.com/doi/10.1002/anie.7709103 by Rüdiger Klingeler - Universitatsbibliothek Heidelberg , Wiley Online Library on [06/11/2026]. See the Terms and Conditions (https://onlinelibrary.wiley.com/terms-and-conditions) on Wiley Online Library for rules of use; OA articles are governed by the applicable Creative Commons License

53. A. Okazawa, R. Watanabe, M. Nezu, et al., "Ferromagnetic Gd–Cu, Tb–Cu, and Ho–Cu Couplings in Isomorphous [Ln_2Cu] Complexes," *Chemistry Letters* 39 (2010): 1331–1332, https://doi.org/10.1246/cl.2010.1331.

54. R. Watanabe, K. Fujiwara, A. Okazawa, et al., "Chemical Trend of Ln–M Exchange Couplings in Heterometallic Complexes With Ln = Gd, Tb, Dy, Ho, Er and M = Cu, V," *Chemical Communications* 47 (2011): 2110–2112, https://doi.org/10.1039/C0CC04669H.

55. M. Andruh, I. Ramade, E. Codjovi, O. Guillou, O. Kahn, and J. C. Trombe, "Crystal Structure and Magnetic Properties of [Ln_2Cu_4] Hexanuclear Clusters (where Ln = trivalent lanthanide). Mechanism of the Gadolinium(III)-Copper(II) Magnetic Interaction," *Journal of the American Chemical Society* 115 (1993): 1822–1829, https://doi.org/10.1021/ja00058a029.

56. A. Bencini, C. Benelli, A. Caneschi, R. L. Carlin, A. Dei, and D. Gatteschi, "Crystal and Molecular Structure of and Magnetic Coupling in Two Complexes Containing Gadolinium(III) and Copper(II) Ions," *Journal of the American Chemical Society* 107 (1985): 8128–8136, https://doi.org/10.1021/ja00312a054.

57. G. Rajaraman, F. Totti, A. Bencini, A. Caneschi, R. Sessoli, and D. Gatteschi, "Density Functional Studies on the Exchange Interaction of a Dinuclear Gd(iii)–Cu(ii) Complex: Method Assessment, Magnetic Coupling Mechanism and Magneto-Structural Correlations," *Dalton Transactions* 38 (2009): 3153–3161, https://doi.org/10.1039/b817540c.

58. J. Arneth, X. F. Li, J. Braun, et al., "The Interplay of Single Ion Anisotropy and Magnetic 3 *d*-4 f Interactions in $V^{III}{}_2Ln^{III}{}_2$ Butterfly Complexes," *Chemistry Europe* 3 (2025): e202500011, https://doi.org/10.1002/ceur.202500011.

Supporting Information

Additional supporting information can be found online in the Supporting Information section.

Supporting File: anie75551-sup-0001-SuppMat.docx.

15213773, 0, Downloaded from https://onlinelibrary.wiley.com/doi/10.1002/anie.77091O3 by Rüdiger Klingeler - Universitätsbibliothek Heidelberg , Wiley Online Library on [06/11/2026]. See the Terms and Conditions (https://onlinelibrary.wiley.com/terms-and-conditions) on Wiley Online Library for rules of use; OA articles are governed by the applicable Creative Commons License